ATOMIC WEAPON DATA
Category Sigma 1
LA-4919

USAEC, Headquarters Library, Reports Section, Washington, D. C.	1-3
Division of Military Application, Washington, D. C.	4
Attn: Col. Henry W. Parlett	
Manager, ALO, Albuquerque, New Mexico	5
Attn: Myron Roepke	
Lawrence Livermore Laboratory, Livermore, California	6-7
Attn: Robert daRoza	
Sandia Corporation, Albuquerque, New Mexico	8
Attn: Charles Winter	
Military Liaison Committee, Washington, D. C.	9
Director, Defense Research and Engineering, Washington, D. C.	10
Headquarters, Defense Nuclear Agency, Washington, D. C.	11-12
Defense Nuclear Agency Field Command, Kirtland AFB, New Mexico	13-15
Commanding General, Army Combat Developments Command, Fort Belvoir, Virginia	16-17
Commanding General, Army Materiel Command, Washington, D. C.	18
DCS/Operations, Army, Washington, D. C.	19
Chief, R&D, Army, Washington, D. C.	20
Naval Ordnance Systems Command, Washington, D. C.	21
Chief of Naval Operations (OP-75), Washington, D. C.	22
Naval Research Laboratory, Washington, D. C.	23
Attn: Keith W. Marlow	
DCS/Research and Development, Headquarters, USAF, Washington, D. C.	24
Director, Air Force Weapons Laboratory, Kirtland Air Force Base, New Mexico	25-27
Space and Missile Systems Organization, Los Angeles, California	28-47
Attn: Lt. Col. Clement/Lt. Holliday	
Los Alamos Report Library	48-75

CONTENTS

b(1)

LIST OF TABLES

LIST OF FIGURES

The motivation for the strategic designer perhaps lies in an increase by a factor of three or four in yield-to-weight ratios, but the probability of successful deployment of such a weapon in the 1970-1980 period is low and unpredictable. Because of this uncertainty, the design of an inspection system should not be influenced strongly by characteristics

Assuming typical and current weapon technology, the important criteria for detection and identification can be listed. While the order of listing is not necessarily significant, two categories are used which to some extent separate the detection and identification criteria from those of acquiring significant additional intelligence data. Obviously there is considerable overlap in these two categories as well as in the individual criteria. Some items as listed are not entirely separable except under the limitations of specific techniques, nor are all items relevant to all potential warheads. However, all are discernible to some degree by the inspection methods proposed in this report.

(1) (a) Unique identification of the essential fission and fusion fuels: ^{235}U, ^{238}U, ^{239}Pu, and deuterium.

(b) Determination of approximate quantity and distribution of fissile and fusion fuels,

(c)

(2) (a) Identification and configuration of high-Z materials in nuclear components and radiation case.

(b) Determination of radiation channel, HE, and RV configurations.

(c) Measurement of approximate attenuation of system in unique locations.

(d) Identification of RV- and warhead-hardening techniques.

(e) Determination of significant fuzing and firing details that might be associated with boosting or safing components.

(f) Measurement of nuclear material isotopic ratios for production cycle information.

(g) Determination of reactivity of subcritical configurations by dynamic response.

These criteria, if completely determinable, would give high confidence to any statement as to the presence of nuclear warheads and would with reasonable confidence add to the completeness and accuracy of current US estimates of foreign weapon technology. The complexity of the list requires a combination of techniques to maximize the chance of obtaining reliable data on any given target. As will be seen later in the correlation of sensor packages to detection criteria, the overall success rate is related directly to the number and sophistication of the detection techniques employed and to the relative absence of countermeasures.

IV. Countermeasures

b(1)

V. Detection Techniques

A. Passive Gamma Technique.

1. Characteristic Gamma Signature of Weapons Materials. The major characteristic signatures of the various radioactive weapon materials will be discussed only briefly. The reader is assumed to have a basic knowledge of these signatures and the decay chains involved.

Characteristic ^{238}U lines at 766.4 and 1001.0 keV arise from the ^{234m}Pa daughter which attains equilibrium in about three months after chemical purification of the uranium.

Data to be shown later will also illustrate the strong view-angle dependence of these spectra.

These spectra indicate that the lines that can be used for isotopic identification in practical cases are the characteristic plutonium and ^{238}U lines. The 2614-keV line is there, but its presence, in general, cannot be unambiguously assigned to a specific isotope, because it can be observed from 93.5% ^{235}U, ^{239}Pu, and ^{232}Th.

3. Experimental Results. The major experimental gamma-spectroscopy effort in this program was devoted to measuring photopeak fluxes from various US weapons systems as a function of distance and view angle. A discussion of some characteristics of Ge(Li) detectors is relevant to the effort and is given separately in Appendix A. The measurements were made with 6% Ge(Li) and 3- by 3-in. NaI detectors, and net counts in each photopeak were obtained by subtracting a linear extrapolation of the Compton continuum from underneath the photopeak. The efficiency curves of the appendix were then used to convert net photopeak counts to photopeak flux.

For the NaI data, the 400-keV ^{239}Pu complex appears as one peak. The flux was computed for the entire complex using the detector efficiency value at 400 keV. The high resolution data of Cline[7] shows that the 375- and 414-keV thin sample intensities are equal. The sum of the 375- and 414-keV intensities in turn is equal to approximately one-half the total intensity between 300 and 450 keV, the range covered in the NaI peak. With these arguments for a basis, the 375- and 414-keV photopeak fluxes or counting rates were approximated by taking each to be equal to one-fourth of the total flux in the 400-keV complex. This approximation neglects minor differences in attenuation in the weapon; however, these differences tend to be cancelled in the detector counting rate because of the slope of the detector efficiency curve.

Data were taken at LASL on the W-59 in its shipping container with both NaI and Ge(Li) detectors in a 33° FOV geometry. Measurements as a function of distance out to about 30 ft were made at four different view angles. For two of the view angles both Ge(Li) and NaI data were taken. In Fig. 7, a comparison of the Ge(Li) and NaI data is shown for the 375- and 414-keV lines as well as for the entire 400-keV complex. The view angle here is looking at the center of the channel at a 45° angle between the side and the primary end of the device. A similar comparison for the D-38 lines for side incidence is shown in Fig. 8.

Fig. 7.
W-59 photopeak flux vs distance, plutonium photopeaks, NaI and Ge(Li) detectors.

The scatter of the points is indicative of the magnitude of errors that arise in the measurement,

Fig. 8.
W-59 photopeak flux vs distance, ^{238}U photopeaks, NaI and Ge(Li) detectors.

TABLE V

PHOTOPEAK FLUX VS VIEW ANGLE, W-59 AT 20 FT

Flux ($\gamma/cm^2/sec$)

These studies were carried out on four different designs (W-62, W-68, Mk-53, Mk-43) at Pantex and Figs. 9 through 11 show the results of some of the measurements, all taken with a 3- by 3-in. NaI detector in 51° FOV geometry. Typical spectra from which these data points were extracted are shown in Figs. 12 through 16.

These illustrated spectra were all taken at 20 ft for count times of 10 to 20 min and represent realistic spectra that would be obtained in a low background inspection for reasonable counting times if a 3- by 3-in. NaI detector were used. The results of the flux measurements for a distance of 20 ft are tabulated in Table VI.

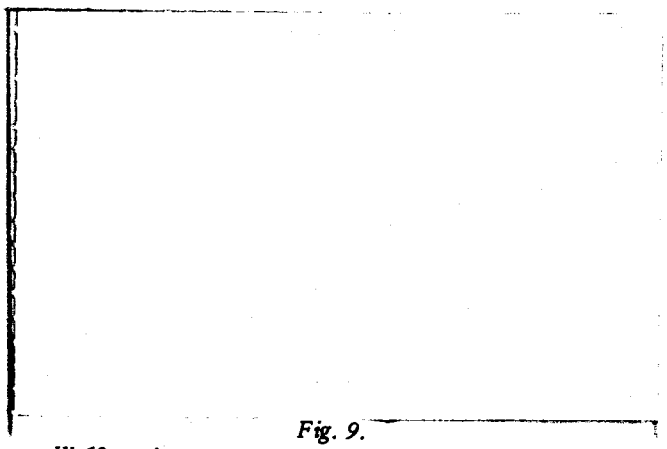

Fig. 9.
W-62 and W-68 photopeak flux vs distance, ^{239}Pu and ^{238}U photopeaks, NaI detector.

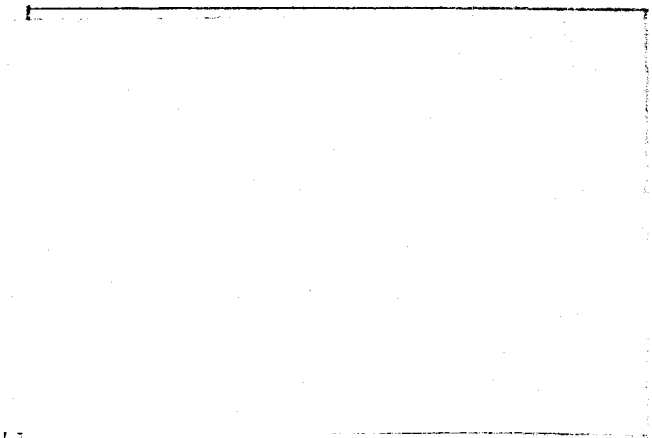

Fig. 10.
Mk-43 photopeak flux vs distance, ^{239}Pu and ^{238}U photopeaks, NaI detector.

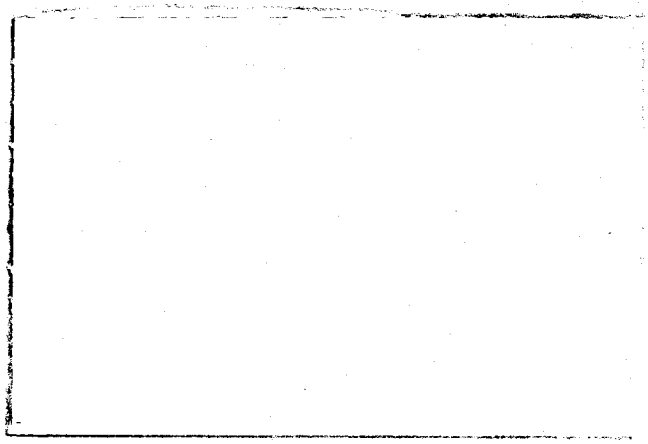

Fig. 11.
Mk-53 photopeak flux vs distance, ^{238}U photopeak, NaI detector, end-on view of secondary.

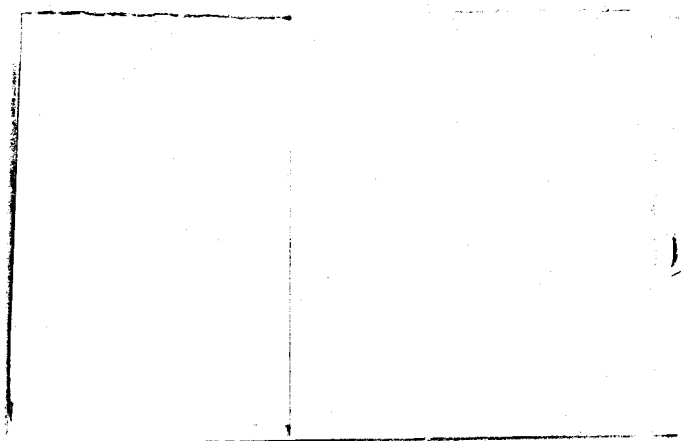

Fig. 12.
W-68 gamma spectrum, 3- by 3-in. NaI at 20 ft, 10-min count.

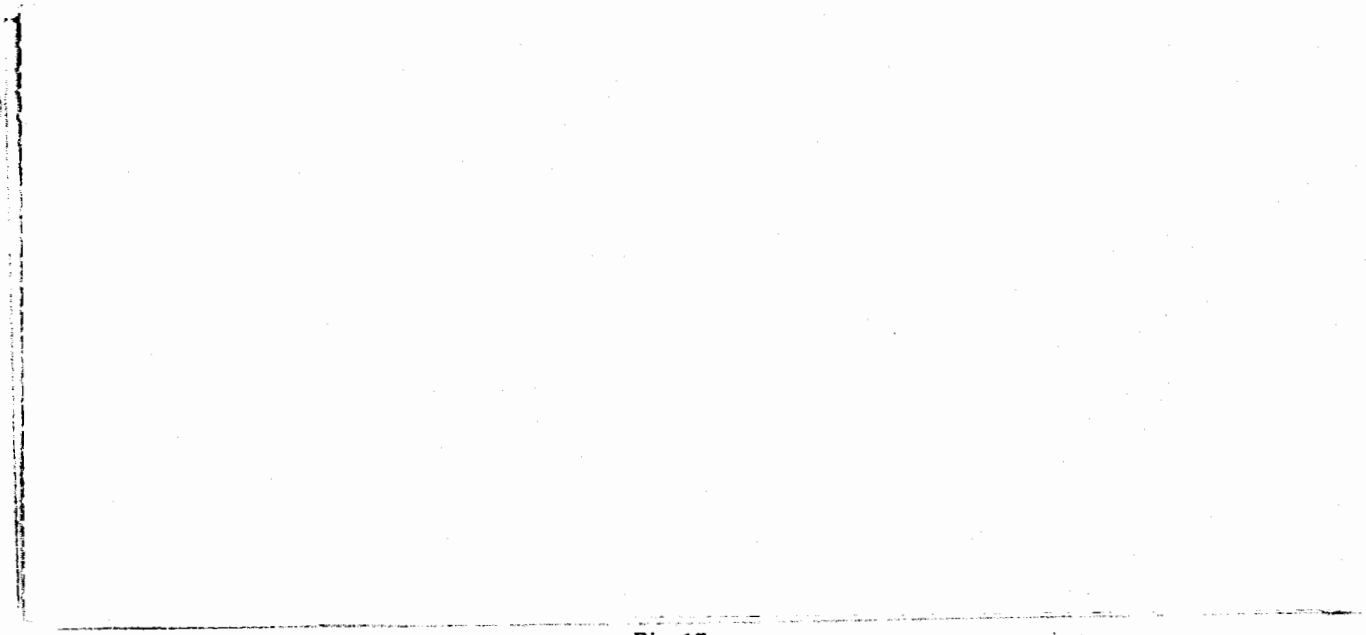

Fig. 17.
W-68 characteristic x-ray spectrum, primary end.

B. Passive Neutron Detection. The significant neutron emitters among common weapons materials are ^{238}U and ^{240}Pu, and these isotopes emit approximately 0.014 n/g-sec and 900 n/g-sec respectively from spontaneous fission.

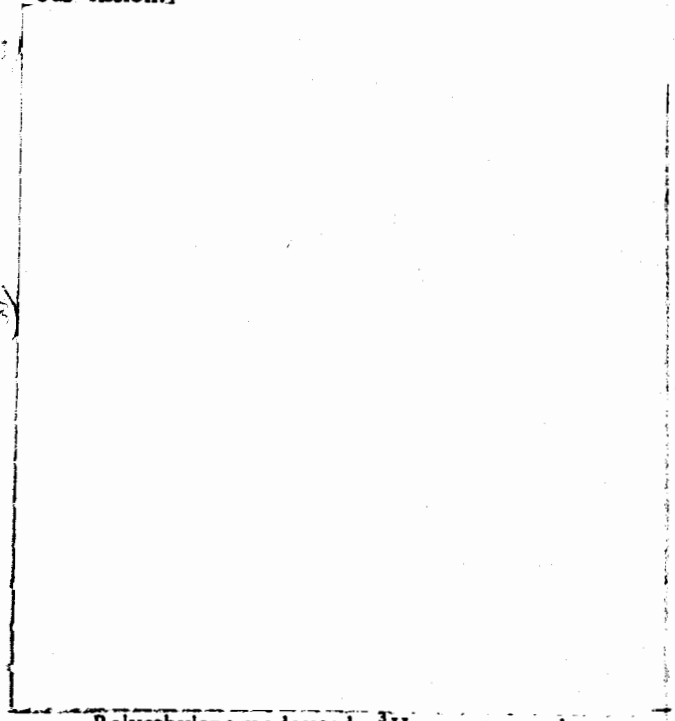

Polyethylene-moderated ^{3}He neutron detectors have been developed with intrinsic efficiencies for 1-MeV neutrons of nearly 20%.[8,13,14] For example, a detector of this type (19 ^{3}He tubes in a 20- by 24- by 3-in. polyethylene matrix) was used to detect neutrons from the W-59. The count rate as a function of distance for a side-on position is shown in Fig. 18. For this detector, the local background ranges from 5 to 10 cps.

While passive neutron detection is desirable, it is also redundant since passive gamma techniques give a more positive indication of the presence of ^{239}Pu. However, passive neutron detection is provided as an option for little cost by using the neutron detector proposed for

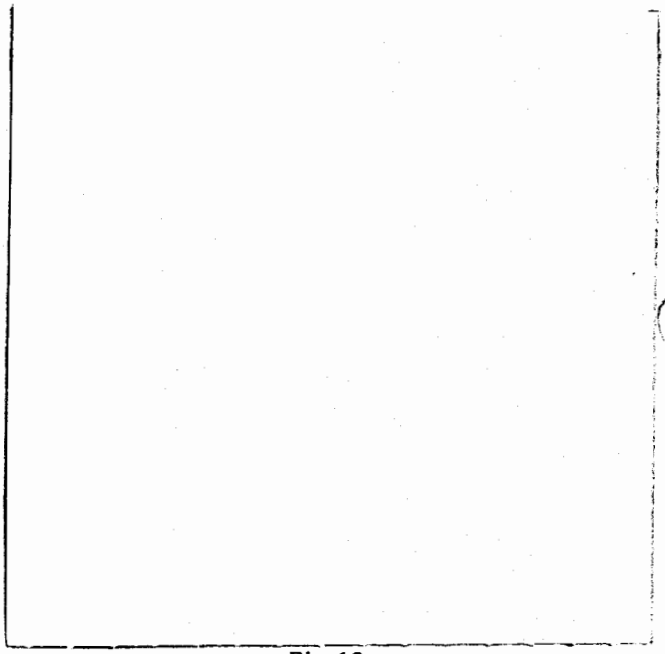

Fig. 18.
W-59 neutron count rate vs distance, 20- by 24- by 3-in. moderated ^{3}He detector.

TABLE XII

(γ,n) COUNTING PARAMETERS FOR 500-Ci SOURCE

Warhead	Yield (Mt)	Net Counts and Statistical Error with 20 cps BKG	Net Counts and Statistical Error with 200 cps BKG	Average Neutron Energy (Mev)
		1880 ± 64	1880 ± 88	1.1
		1880 ± 63	1880 ± 87	~ 1.0
		4520 ± 97	4520 ± 114	0.05
		1120 ± 51	1120 ± 79	~ 0.10
		1960 ± 66	1960 ± 89	~ 0.05
		3640 ± 88	3640 ± 106	~ 0.05

b. Relative Photonuclear Yields. A general feature of bremsstrahlung-induced reactions is a steep rise in yield as a function of increasing electron energy above the reaction threshold: This phenomenon is illustrated in Fig. 40 which shows the bremsstrahlung-induced photoneutron yields for a variety of small samples over the electron energy range from 5 to 15 MeV. These measurements were made at the LASL electron prototype accelerator (EPA) with a slab-type neutron detector. Up to about 10 MeV the yields for D_2O and beryllium dominate. Above this energy photofission yields dominate. Below about 8 MeV the photoneutron yields of such high-Z materials as bismuth and lead are negligible if ^9Be, ^2D, or fissionable isotopes are present. The photoneutron yields of intermediate-Z materials such as copper and iron are negligible at all energies of interest.

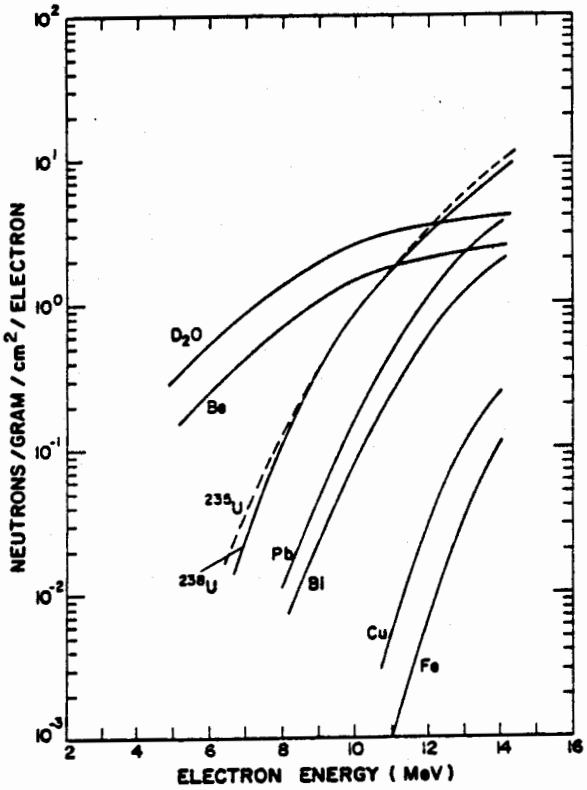

Fig. 40.
Relative bremsstrahlung-induced photoneutron yields for several materials.

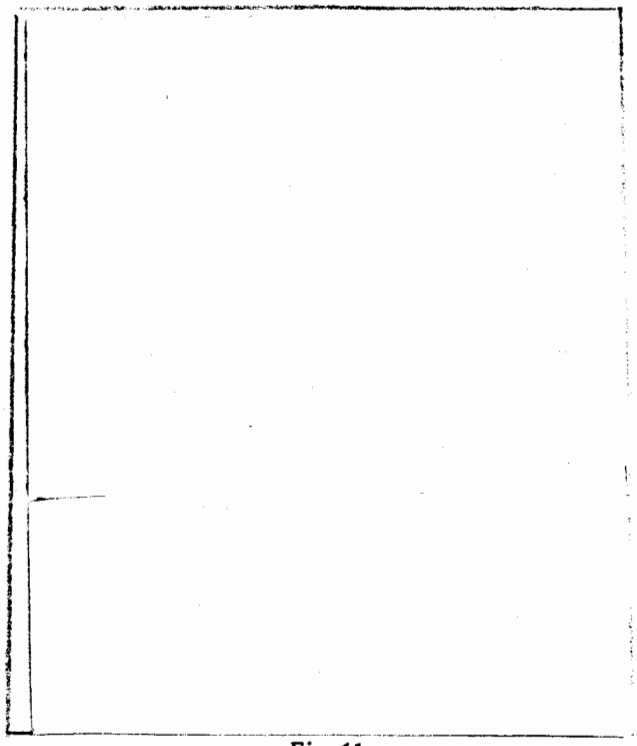

Fig. 41.
Photoneutron yield as a function of electron energy for three classes of weapon secondaries.

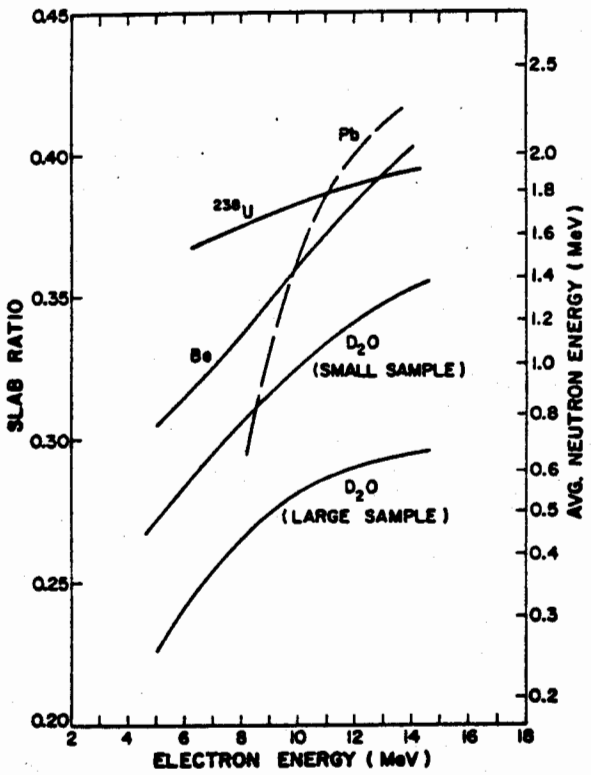

Fig. 42.
Slab-ratio data for bremsstrahlung-induced photoneutron reactions.

c. Photoneutron Spectra. The problem of beryllium determination and secondary design identification can also be approached through photoneutron spectral measurements. The description of photoneutron spectra in detail is complex; however, one general feature is a monotonic increase in average neutron energy with increasing electron energy. This is illustrated in Fig. 42 for beryllium, deuterium in heavy water samples, lead, and ^{238}U over the electron energy range 5 to 15 MeV. These measurements were made at the EPA using the slab-ratio method. As can be seen ^{9}Be has a considerably higher average neutron energy than ^{2}D for all electron energies. The average energy for a large D_2O sample is also shown in Fig. 42

The ^{238}U average energy is reasonably constant with electron energy, as expected for the fission process. This average neutron energy would also be obtained approximately for other photofissionable isotopes such as ^{235}U, ^{239}Pu, and ^{232}Th and for neutron-induced fission spectra.

b(1)

When higher energies are used, the photofission neutrons of ^{238}U, ^{235}U, and ^{239}Pu can be used for weapons detection. Figure 49 shows the ^4He spectrometer measurements of small sample ^{238}U photofission neutrons. Pulse-height distributions are shown for 6-, 7-, 10-, 12-, and 15-MeV electrons and are normalized to the same approximate bremsstrahlung dose incident on the sample at each electron energy. If the curves are multiplied by $(E_e)^3$ at each electron energy, they will be expressed approximately on a relative scale per electron.

The D(γ,n) distribution for 6- to 15-MeV electrons, also plotted for equal doses at each electron energy, is shown in Fig. 50. The systematic change of the spectral endpoint can be easily seen. Figure 51 shows a comparison of ^{238}U and Pb(γ,n) signatures at 10 MeV and

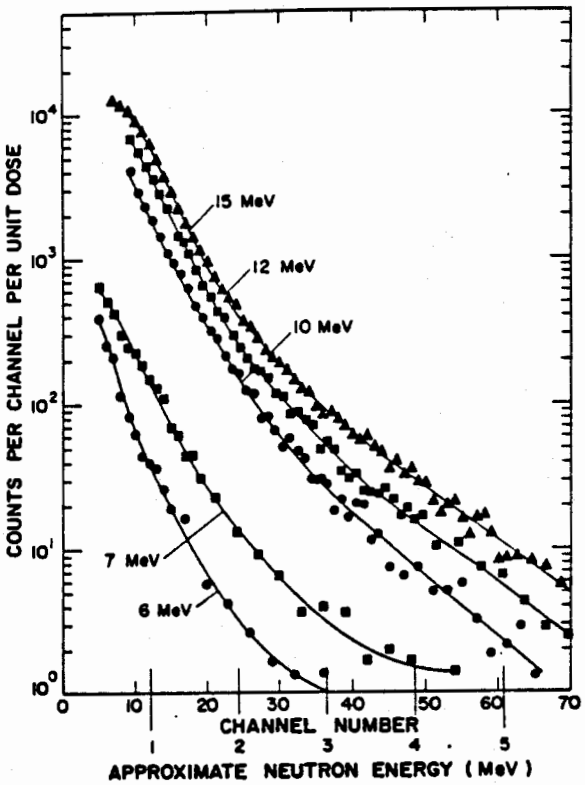

Fig. 49.

^4He neutron spectrometer data, ^{238}U photoneutron and photofission neutron pulse-height distribution for various bremsstrahlung energies.

illustrates a possible means of distinguishing between conventional and clean secondary designs.

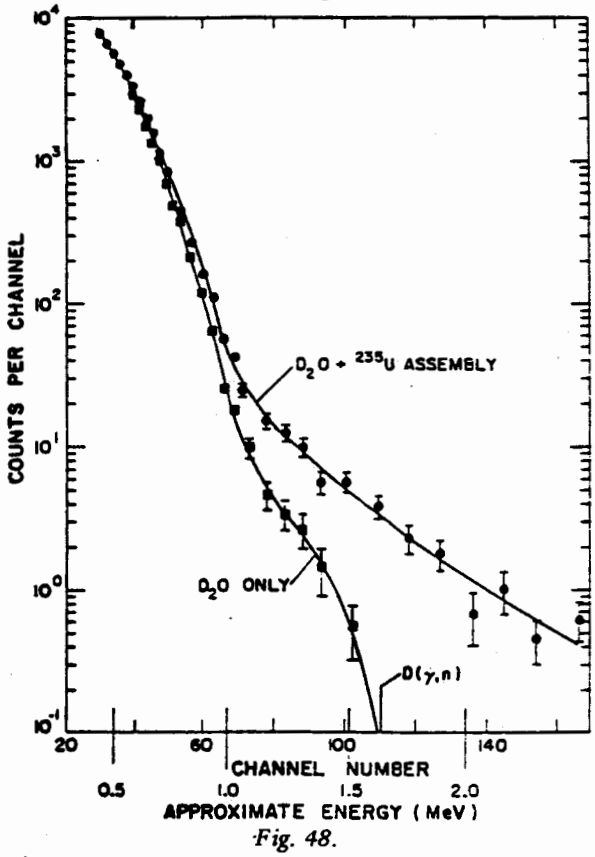

Fig. 48.

^4He neutron spectrometer data, 5.5-MeV bremsstrahlung-induced photoneutron pulse-height distribution for D_2O and for D_2O plus ^{235}U assembly.

UNCLASSIFIED

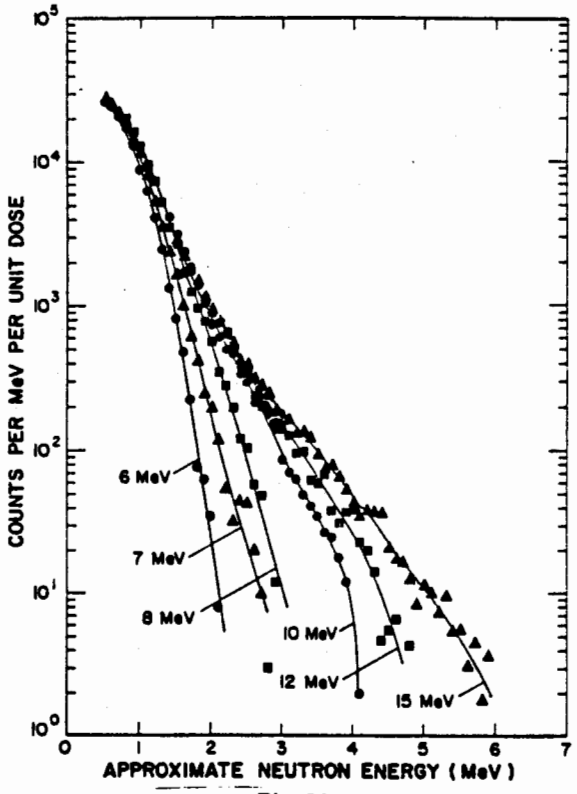

Fig. 50.
D(γ,n) ^{4}He proportional counter pulse-height distribution for 6- to 15-MeV bremsstrahlung.

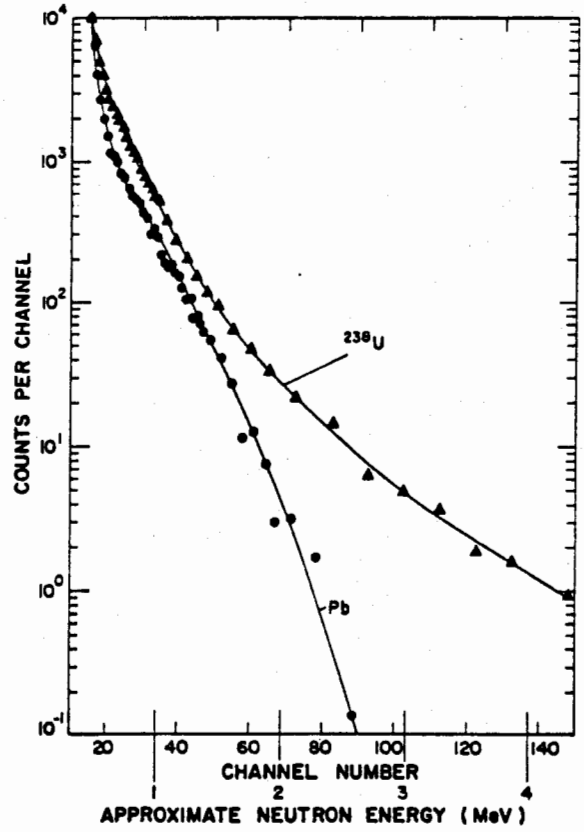

Fig. 51.
10-MeV bremsstrahlung-induced photoneutron pulse-height distribution for lead and ^{238}U.

b(2)
b(1)

[redacted]

one for larger quantities of beryllium.

d. Calculated and Scaled Results. To some extent the various results presented above can be summarized by scaling to the same systems described in Table XII for the radioisotope (γ,n) results. Anticipating the system definitions presented in detail in Sec. VI, two specific source and detector combinations are selected.

Table XV shows the number of counts obtained for various weapons using a Marx generator flash x-ray source at several energies and the slab detector described earlier. The Marx generator and the neutron detector are assumed to be 20 ft from the weapon. The net counts shown are for 40 pulses of 1.25×10^{14} electrons each (each pulse is thus equivalent to 100 A for 0.2 μsec). These calculated values are based on small sample measurements, radioactive source (γ,n) measurements, and the attenuation and multiplication calculations mentioned above. The expected count from beryllium in small RV quantities is also shown. For beryllium in this quantity or less, a few pulses at 2.2 MeV would suffice to determine beryllium effects to ± 20%. However, this technique is not a good

Because Marx generator measurements would be pulsed, the effects of space backgrounds would be small. Assuming the backgrounds previously discussed and a 50-μsec counting time per pulse, the total background count from all sources during the 40-pulse irradiation (Table XV) would be less than one count.

Table XVI shows bremsstrahlung-induced count rates expected for a photointerrogation system using a 500-W, 5-MeV electron linac. This beam is incident on a thick (≈ 0.10 cm) tungsten bremsstrahlung target assumed to be 10 ft from the interrogated weapon. The linac is farther away with the bremsstrahlung target suspended on a lightweight boom. The detector is assumed to be a bank of 10 16-atm ^{4}He proportional counters (2 in. diam, 24 in. long) located 20 ft from the interrogated weapon.

The entries in Table XVI were obtained by scaling measured D(γ,n) ^{4}He spectrometer count rates from the EPA small sample measurements to the ^{6}LiD mass distribution appropriate to each weapon. Complicating effects such as bremsstrahlung attenuation in intervening high-Z

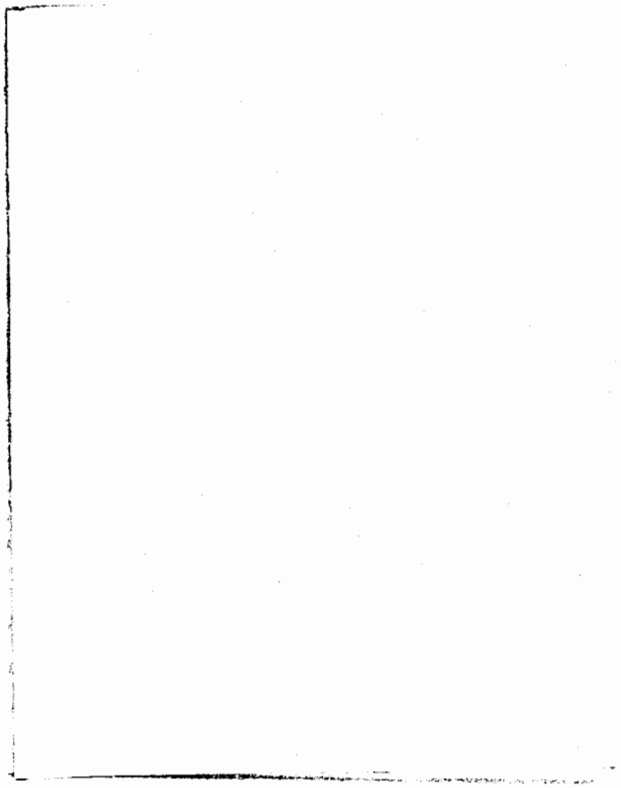

Fig. 52.
Linac interrogation of the Mk-53 for electron energies of 6 to 12 MeV.

materials and ^{235}U (n,f) reaction components were taken into account using the techniques described in Ref. 9. The resulting output spectrum (analyzed approximately into separate D(γ,n) and ^{235}U (n,f) components) was then folded into the ^{4}He detector response, and the final spectrometer response was summed over the indicated limits to illustrate approximate statistical accuracies for various pulse-height ranges. The beryllium-only entry was calculated in a similar fashion assuming that 2.5×10^{3} cm^2 of beryllium, 0.07 cm thick, is on the exterior portion of the target weapon.

The effect of space background on these measurements is negligible, primarily because the linac is pulsed, and the indicated 100-sec interrogation corresponds to a detector on-time of about 0.5 sec. Using the space neutron background estimates already discussed, about 4 to 40 total counts can be expected, distributed over the entire pulse-height range 0 to $>$ 10 MeV. This background could probably be neglected entirely; however, an *in situ* background measurement between beam bursts could easily be made.

Electronics for the ^{4}He spectrometer are identical to those discussed earlier for the ^{3}He slab detector with the exception that a pulse-height analyzer is also required. Only a modest number of channels of pulse-height data are required ($\sim$ 100), and the pulse-height analyzer discussed in connection with the passive gamma detector is more than adequate for this purpose.

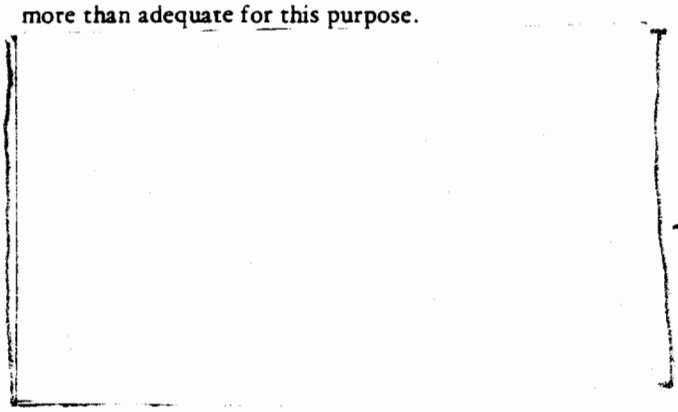

The spectra of Fig. 52 can be converted to the conditions of Table XVI by simple scaling

TABLE XV

APPROXIMATE SLAB DETECTOR COUNT RATES FOR 40 PULSES OF A MARX GENERATOR WITH 100-A, 0.2-μsec PULSES

Weapon	4-MeV Electrons (Net Counts)	5-MeV Electrons (Net Counts)	2.2-MeV Electrons (Net Counts)
	474	1452	—
	454	1390	—
	1140	3490	—
	282	866	—
	494	1514	—
	918	2812	—
	474	1058	50

TABLE XVI

APPROXIMATE COUNTS OBTAINED WITH A 100-SEC, 5-MeV LINAC INTERROGATION OF SELECTED WEAPONS SYSTEMS

Weapon System	Counts ⩾ 0.5-MeV Pulse Height	Counts ⩾ 1.0-MeV Pulse Height	Counts ⩾ 1.39-MeV Pulse Height [D(γ,n) Endpoint]	Counts ⩾ 2.96-MeV Pulse Height [Be(γ,n) Endpoint]
	5000	1970	960	120
	7300	1000	35	4
	4800	1890	920	110
	1800	250	9	1
	5880	800	28	3
	1000	260	70	—

Experiments to compare relative 14-MeV neutron and 10-MeV electron bremsstrahlung-induced fission efficiencies were performed on a Mk-53 at Pantex in a standard geometry using the same neutron detector.

4. Delayed Fission Neutron Time History. Delayed neutrons are a unique signature for fissionable isotopes at 10 MeV because there are no other photoreactions on any isotope that can generate directly a delayed neutron. In addition, under favorable conditions the delayed neutron time history from photofission can be used to determine a rough $^{235}U/^{238}U$ isotope ratio.

Figure 53 shows a delayed neutron time history for the Mk-53 system following 10-MeV bremsstrahlung-induced photofission.

Figure 54 shows the delayed neutron time history for a 7-MeV bremsstrahlung irradiation of the XW-67 secondary. This measurement was done at the SCAPP at LASL, and the data shown are the sums produced by 10 0.2-μsec pulses spaced 30 sec apart. Again, a slab detector was used. The solid line through the data points is the calculated time history using published ^{235}U (n,f) delayed neutron time history parameters.[22] The dashed line is the calculated time history using published small sample ^{235}U

Fig. 53.
Mk-53, 10-MeV bremsstrahlung-induced delayed neutron time history.